Towards an interpretation of the scale diffusivity in liquid atomization process: An experimental approach

Christophe Dumouchel, Thibaut Ménard, Wojciech Aniszewski

TOWARDS AN INTERPRETATION OF THE SCALE DIFFUSIVITY IN LIQUID ATOMIZATION PROCESS: AN EXPERIMENTAL APPROACH

Christophe Dumouchel, Thibaut Ménard, Wojciech Aniszewski

CORIA – UMR 6614

Normandie Université, CNRS, Université et INSA de Rouen

Avenue de l'Université, BP 12

76801 Saint-Etienne du Rouvray, FRANCE

Abstract

Recent investigations have presented an application of the scale entropy diffusion theory to model liquid atomization process. This theory describes multi-scale behavior by a diffusion equation of the scale entropy function. In atomization, this function is related to the scale-distribution which provides a measurement of the specific-length of the eroded liquid system according to the scale of erosion. The present paper performs a detail description of the scale diffusion mechanism for the atomization process of a liquid jet emanating from a gasoline injector with the objective of determining the scale diffusivity parameter introduced by the diffusion theory. The 2-D description of the gasoline jet as a function of the injection pressure reveals that the scale space is divided in two regions according to the sign of the scale specific-length variation rate: The small-scale region refers to the scales that undergo an elongation mechanism whereas the large-scale region concerns the scales that undergo a contraction mechanism. Furthermore, two phases of the atomization process are identified depending on whether the elongation mechanism is governed by the jet dynamics or surface

tension effects. A non-dimensional number segregating these two phases is established. During the atomization process, the contraction mechanism diffuses in the small scale region. This manifests by a temporal decrease of the scale with a zero specific-length variation. It is found that the scale diffusivity parameter can be determined from the evolution of this characteristic scale in the second phase of the atomization process.

Keywords: Liquid atomization process, multi-scale analysis, scale entropy diffusion model

1 Introduction

The atomization of a liquid jet ejected into a gaseous environment is a process during which the jet deforms and fragments until a flow of stable droplets of different size and velocity, called a spray, is formed. The prediction of the spray drop-size distribution has always been considered as an important issue and still requires specific investigations aiming to develop liquid atomization models. Visualizations found in the literature demonstrate the multi-scale nature of atomization processes. The fractal concept due to Mandelbrot [1] was convoked to describe the tortuosity of the atomizing system contour [2, 3]. It reported that atomizing liquid systems require a scale and time-dependent fractal dimension to be fully described. This deviation from pure fractality has been pointed out for different systems and a specific geometrical framework to describe these systems and their temporal evolution has been introduced by Queiros-Conde [4] in the context of turbulent interfaces. Derived from the entropic-skins geometry formalism [5], this model defines the scale entropy function to describe the system and uses a diffusion equation to model its temporal evolution. Similar to a 1-D heat diffusion equation with a local heat production term, this scale entropy diffusion equation introduces the concepts of scale diffusivity and of scale entropy flux sink or scale-evolutivity. The scale diffusivity defines the capacity for the system to propagate perturbations through scale-space [6] and the scale-evolutivity describes variation of the evolutive potential (i.e., the scale entropy flux) of the system. The scale entropy diffusion model has been applied to turbulent interfaces and turbulent flames [4, 7]. Among other results, an expression for the scale diffusivity has been established for turbulent interfaces.

In the context of two-phase flows, the scale entropy diffusion model has been applied on a liquid spray [8] and on the atomization of a liquid sheet [9, 10, 11]. The analysis of a liquid sprays revealed a constant scale entropy flux gradient through scale space which corresponds

to a parabolic behavior for scale analysis [8]. In the description of the liquid sheet atomization, it has been evidenced that the scale entropy function can be obtained from the cumulative scale-distribution $E_2(d)$ introduced in a previous investigation [12]. Performed on 2D images, this distribution is obtained from the application of the Euclidean Distance Mapping (EDM) method which is a "sausage technique" to determine the fractal dimension of a contour [13]. $E_2(d)$ is a measurement of the proportion of surface loss caused by erosion operations at successive increasing scales. Its first-derivative according to the scale is a 2D and generalized version of the concept of specific-area introduced by Evers [14]. The specific-area designates the interface surface per unit liquid volume and the surface energy of a two-phase system is proportional to this quantity. It is therefore relevant in atomization. In the present case, the 2D description reports specific-length quantity and the generalization means that this specific-length is considered as a function of the scale, becoming the scale specific-length. The application of the scale entropy theory to describe liquid sheet atomization revealed that the process of flow deformation, fragmentation and droplet production is associated to a continuous evolution of the scale entropy function [9]. The scale diffusivity was determined and correlated to the experimental operating conditions [10] and a scale parabolic behavior was identified in the small scale region [11].

Although these previous investigations demonstrate the interesting potential of the use of the scale entropy diffusion theory in the context of liquid atomization, they show a limitation: the procedure to determine χ doesn't suit other systems than turbulent liquid sheets. Overcoming this problem requires a good understanding of the scale diffusion mechanism in the context of liquid atomization processes. For this task, the recent introduction of the concept of the scale-diameter could be considered [15]. This length is equal to the inverse of the first derivative of $E_2(d)$. The temporal evolution of the scale-diameters leads to a scale segregation according to their own perception of the whole system evolution. Furthermore, for the case of atomizing

stretched ligaments, the quality of this perception allows identifying the physical mechanisms involved in the breakup process [15].

The present investigation aims to produce a multi-scale analysis of the atomization process of a jet produced by a Gasoline Direct Injector (GDI) with the objectives of reaching a detailed description of the scale diffusion mechanism and of determining the scale diffusivity parameter. Despite the injector is conceived to work in transient conditions and has three identical discharge orifices, the study concentrates on one of the three jets and during the fully open stage of the injector only. Furthermore, the injection pressures are mainly low to ensure exploitable visualizations of the atomization process. Section 2 presents the scale entropy diffusion model and the scale diffusivity parameter. The experimental work is presented in Section 3. The experimental results and their analysis are the subject of Section 4.

2 The scale entropy diffusion model and the scale diffusivity

The scale entropy diffusion model as it is used in the present context has already been presented in previous articles [9, 10] and is summarized here only. This model concerns the temporal evolution of multi-scale systems showing scale- and time-dependent fractal dimensions. At each instant, the system is described by the scale entropy function $\Sigma(x,t)$. This function is a global quantity that monotonously decreases and reaches zero for the outer cutoff scale of the system. The scale entropy can be seen as a quantification of the representativeness of a scale d on the system's morphology: the smaller the scale entropy is, the more organized is the shape of the system at this scale. The diffusion model suggests modeling the temporal evolution of the system by the following diffusion equation [4]:

$$\frac{\partial^2 \Sigma(x,t)}{\partial x^2} - \omega(x,t) = \frac{1}{\chi}\frac{\partial \Sigma(x,t)}{\partial t} \tag{1}$$

The variable x is defined by $x = \ln(d/d_{ocs})$ where d is the scale and d_{ocs} is a characteristic outer cutoff scale of the problem. In turbulence, this scale would be the integral scale. In Eq. (1) the parameter χ is the scale diffusivity and the function $\omega(x,t)$ is the scale entropy flux sink defined by a unit of scale logarithm. It is in fact a scale entropy flux density. Queiros-Conde [4] emphasizes the analogy between Eq. (1) and the one-dimensional heat conduction equation: the scale logarithm x would correspond to the position, the scale entropy Σ to the temperature, the scale diffusivity χ to the thermal diffusivity and the function ω to a quantity proportional to a volumetric heat sink that would be space dependent. In heat diffusion, the local heat flux is proportional to the temperature gradient. In multi-scale system description, the scale entropy gradient corresponds to the scale entropy flux ϕ ($\phi(x,t) = \partial\Sigma(x,t)/\partial x$) that quantifies how scale entropy cascades through scale space. A constant scale entropy flux ϕ in a scale range denotes a self-similarity of the system contour for this scale range and therefore a fractal characteristic [4]. At any time, the model beneficiates from a scale entropy flux condition in the small scale range, i.e., $\lim_{x\to-\infty} \phi(x) = -1$. In 2D, this condition corresponds to a fractal dimension equal to 1 [4].

The scale diffusivity χ introduced in Eq. (1) characterizes diffusion of scale entropy through the scale space. This parameter is related to a scale range quantified by a value of $|x|$ and a diffusion time τ^*, i.e.,

$$\chi = \frac{|x|^2}{\tau^*} \tag{2}$$

τ^* can be interpreted as the characteristic time needed by a perturbation to propagate over the scale range quantified by $|x|$. In turbulence, the diffusion time τ^* between the integral scale l_0 (at which energy is injected) and the Kolmogorov scale l_c (at which energy is dissipated) is $\tau^* = \ln^2(l_c/l_0)/\chi$. According to Queiros-Conde [4] this time must be of the order of the dissipation time t_η. Indeed, if $\tau^* < t_\eta$, then energy would accumulate in space scale since dissipation is not efficient enough. Conversely, if $\tau^* > t_\eta$, energy would dissipate completely before reaching the Kolmogorov scale. Thus, assuming $\tau^* \approx t_\eta$, Queiros-Conde [4] derived the following estimation of the scale diffusivity:

$$\chi \approx \left[\frac{9}{16} Re^{3/2} (\ln Re)^2\right] \Big/ \left(l_0^2/\nu\right) \tag{3}$$

where ν is the kinematic viscosity and the Reynolds number Re is based on the integral scale and on the RMS of velocity fluctuation. Such a scenario has not been established for liquid atomization processes.

A previous investigation [9] has reported that the scale entropy for an atomizing liquid system can be derived from the surface-based scale-distribution $E_2(d,t)$ [12], i.e.:

$$\Sigma(x,t) = \ln\left(\frac{1}{E_2(d,t)}\right) \tag{4}$$

Using Eq. (4), the temporal evolution of the scale entropy for experimental turbulent liquid sheet at low Weber number was established [9]. As said in the introduction, the scale entropy reports a continuous evolution all over the process including the flow production, deformation, fragmentation and drop production. In [9], the specific evolution of the scale

entropy flux allowed deriving a procedure to estimate the scale diffusivity χ. It appears that χ increased linearly with the injection pressure ΔP_i. The inverse of the slope of this evolution has the dimension of a dynamic viscosity and is called the scale "viscosity" μ*:

$$\mu^* = \frac{1}{\mathrm{d}\chi/\mathrm{d}\Delta P_i} \tag{5}$$

Furthermore, a correlation between χ and the operating conditions was established [10]:

$$\chi = 2.9 We_L^{0.555} \left(\ln\left(\frac{We_L}{67} \right) \right)^2 \frac{\sigma}{\mu^* d_{or}} \tag{6}$$

The liquid Weber number We_L is defined as $(\rho_L V_q^2 d_{or})/\sigma$ where ρ_L is the liquid density, V_q is the flow rate mean-velocity, d_{or} is the diameter of the discharge orifice and σ is the liquid surface tension. There is a notable similarity between Eqs. (3) and (6): the Reynolds number in turbulence has been replaced by a Weber number in atomization. The last ratio in Eq. (6) is similar to the inverse of the characteristic time of a liquid thread subject to a viscosity controlled thinning process [16].

3 Experimental setup and optical diagnostic

3.1 Experimental setup

The experimental setup is a traditional injection test bench for Gasoline Direct Injection (GDI) application and is similar to the one used in a previous investigation [17]. The liquid is pumped from a reservoir thanks to a combination of a low pressure pump and a high pressure pump. This arrangement provides an absolute pressure ranging from 0 to 16 MPa. The

pressure is regulated and measured by a high pressure sensor just before the injector. This measured pressure is the one referred as the injection pressure ΔP_i. The experiments were performed under atmospheric ambient pressure and temperature.

The injector is a three-jet GDI device. It is conceived to work in transient conditions and it is equipped with a needle that controls its opening and closing. In the closing position, the needle rests on the wall of the nozzle sac volume. The injector opening is controlled by a unit that is set in order that the needle reaches the maximum possible lift in every working condition. The nozzle discharge orifices are located at the bottom of the sac volume. The injector has three identical orifices with a diameter d_{or} = 250 µm. They are regularly distributed at the nozzle tip and make an angle of 42° with the axis of the injector body. The maximum injection pressure tolerated by the injector is 12 MPa. In the present work, the injection pressure range is restricted to [0.1 MPa; 2.5 MPa].

The liquid used is Shellsol D40 whose physical properties are: density ρ_L = 766 kg/m^3; surface tension σ = 0.025 N/m; dynamic viscosity μ_L = 0.9 10^{-3} Pa.s. The volume flow rate of the fully open stage, i.e., when the injector needle is maintained in its upper position, is measured as a function of the injection pressure according to the protocol detailed in a previous work [17]. For the present injection pressure range, these measurements reported a constant discharge coefficient C_D = 0.47. From this value, a mean flow-rate velocity V_q can be calculated by:

$$V_q = C_D \sqrt{\frac{2\Delta P_i}{\rho_L}} \tag{7}$$

Using this velocity, the Reynolds number ($Re = \rho_L V_q d_{or}/\mu_L$) and the gaseous Weber number ($We_G = \rho_G V_q^2 d_{or}/\sigma$ where ρ_G is the gas density) of the flow issuing from one injector orifice

are calculated. The maximum values for *Re* and We_G are 8000 and 19, respectively. The critical We_G above which aerodynamic forces have a non-negligible effect on the spray scale distribution is of the order of 3 to 5 for liquids whose surface tension varies from 0.02 N/m to 0.07 N/m [10]. These results indicate that, in the present work, the action of the aerodynamic forces is indisputable for $\Delta P_i > 0.6$ MPa.

3.2 Visualization technique and Image processing

Snapshots of the liquid flow issuing from the injector have been taken. A shadowgraph optical arrangement was chosen, i.e., the light source, the object and the camera are aligned and the image of the object shadow is recorded. The light source was a Nanolite HSPS whose flash duration is of the order of 20 ns. In the present configuration, the light source plays the role of the shutter. The receiver was a Kappa Camera (1380x1028 pixels). The injector was positioned so that a single jet among the three was visualized and that the top of the image coincided with the bottom of the injector, which is 1 mm below the discharge orifice exit plane. The field covered by the image is 6 mm x 8 mm. The corresponding spatial resolution is equal to 5.8 µm/pixel. At the maximum injection pressure (2.5 MPa), the velocity V_q (Eq. (1)) is equal to 38 m/s. At this velocity, the displacement during 20 ns is equal to 0.8 µm corresponding to 0.14 pixel. The optical arrangement is appropriate to provide frozen liquid flow images in all cases. As said in the introduction, the liquid jet behavior issuing from the injector during its fully open stage is investigated only. To ensure this, the injection time is set at 9 ms and a single image is taken at 8 ms after the injection command. For every working condition, a total of 250 images were taken and analyzed.

The analysis of the atomization process requires two gray-level images. To achieve this, homemade image treatments similar to those presented in previous works [3, 9, 10] and including image normalization, contour detection and corrections have been applied. The

resulting images show the liquid system in white on a black background. Furthermore, in order to ease the local analysis of the liquid system, the images are oriented in order that the jet appears vertical. The resulting images are cropped to cover a 10 mm x 10 mm physical field. As in the initial images, the top of the reoriented image is at 1 mm downstream from the actual position of the discharge orifice exit section.

4 Experimental Results and Analysis

Figure 1 presents raw images of the liquid jet issuing from one orifice discharge as a function of the injection pressure. The quality of the image is good and the flow is well frozen for every injection pressure.

At low injection pressures (first row in Fig. 1), the liquid jet is rapidly and highly corrugated. This corrugation is initiated by the liquid flow internal structures. Indeed, even at low injection pressures, the liquid flow issuing from the injector is not laminar because of the complex injector internal geometry that imposes drastic flow deflections and stresses. Some of the initial perturbations grow and structure the jet shape variation and breakup. This atomization process shows the production of transverse ligaments and the transformation of the bulk as a ligament network. When the injection pressure increases (second row in Fig. 1), more ligaments develop from the bulk flow, increasing the number of droplets. For the highest injection pressures (third row in Fig. 1) the bulk flow is surrounded by droplets and the jet liquid core is more indented. From a general point of view, we see in Fig. 1 that the jet plume broadens when the injection pressure increases, which actually is a mark of a more and more perturbed state. At the same time, structures at smaller and smaller scale develop during the atomization process. Thus, the representative scale interval of the liquid system enlarges with the injection pressure.

The performance of the image treatment procedure can be assessed in Fig. 2 that shows the monochrome-converted images corresponding to the snapshots in Fig. 1. The temporal description of the atomization process is performed on these images by analyzing a portion of the liquid system delimited by a rectangular Analyzing Window (AW) as shown in Fig. 3 and by sliding this AW from the top down to the bottom of the image. The position h of AW, which corresponds to the distance from the discharge orifice exit section plane to the AW middle line, is associated to an equivalent time t (see Fig. 3):

$$t = \frac{h}{V_q} \tag{8}$$

The analysis of the part of the liquid system delimited by the AW consists of measuring the cumulative scale distribution introduced in [12]. This distribution, considered as a local information and noted $E_2(d,t)$, is defined by:

$$E_2(d,t) = \frac{S_T(t) - S(d,t)}{S_T(t)} \tag{9}$$

In this equation, d is the scale of observation, $S_T(t)$ designates the total surface of the liquid system portion delimited by the AW and $S(d,t)$ is the remaining surface after the liquid system portion has been eroded by a circular structuring element with a diameter equal to d. The erosion of the liquid system with a circle of diameter d is illustrated in Fig. 4. In this figure, $S(d,t)$ is the white surface, and $S_T(t) - S(d,t)$, numerator of Eq. (9), corresponds to the hashed surface. When d varies from 0 to infinity, $E_2(d,t)$ monotonously increases from 0 to 1. This function is the cumulative scale function. This measurement is performed on a series of AW positions (from the top down to the bottom of the image) and on the 250 images available for

each working condition. The final local cumulative scale distributions are averages of these 250 measurements for each position.

The first derivative of the cumulative scale distribution introduces the scale distribution $e_2(d,t) = \mathrm{d}E_2(d,t)/\mathrm{d}d$. It represents the perimeter of the eroded system portion at scale d (black line in Fig. 4) divided by its total surface area. It is interesting to note that for $d = 0$, this quantity is similar, in 2D, to the specific surface area introduced by Evers [14]. $e_2(d,t)$ is a more general quantity that represents the specific-length of the system as a function of the scale of observation. The dimension of the scale distribution $e_2(d,t)$ is the inverse of a length. Thus, its inverse is equivalent to a length. This length is called the scale diameter and is noted $D(d,t)$, i.e.:

$$D(d,t) = \frac{1}{e_2(d,t)} \tag{10}$$

The scale diameter $D(d,t)$ can be seen as the width of the rectangle whose height is equal to half perimeter of the eroded system at scale d and whose surface is equal to $S_T(t)$. A decrease of the scale diameter $D(d,t)$ during time for a given scale d could be due to either an increase of the perimeter of the eroded system or a decrease of its surface $S_T(t)$ or a combination of these two possibilities. The increase of the perimeter can be associated to an elongation of the system in the image plane whereas the decrease of the system surface would result from an elongation mechanism in a direction perpendicular to the image plane. In consequence, a decreasing $D(d,t)$ in time is representative of the action of an elongation mechanism. Inversely, an increasing $D(d,t)$ in time is representative of the action of a contraction mechanism. Thus, the temporal variation of the scale diameter gives information on the impact of the system shape variation at each scale: if $\partial D(d,t)/\partial t < 0$, the system shape

variation at scale d is undergone as elongation; if $\partial D(d,t)/\partial t > 0$, the system shape variation at scale d is undergone as contraction.

The cumulative scale distribution is measured on the images with the software ImageJ. A high frequency filter is applied to remove the high frequency variations of the averaged local cumulative scale distributions $E_2(d,t)$. The scale distribution $e_2(d,t)$ is determined from centered scheme formulation. The resulting distributions report a good accuracy all over the scale space. We have to mention however that pixelization may deteriorate this accuracy at scale $d = 0$. However, the error remains less than 10% for this specific scale. Finally, following the protocol defined in a previous investigation [9] the most appropriate AW height is determined. This height is defined as the maximum one below which the scale distribution $e_2(d,t)$ displays no sensitivity to this parameter. In the present configuration, this height is found equal to 140 pixels, i.e., 0.813 mm.

Figure 5 shows a typical temporal evolution of the cumulative scale distribution $E_2(d,t)$ for $\Delta P_i = 0.4$ MPa. This figure illustrates that the atomization process is described by a continuous evolution of $E_2(d,t)$. We see that the smallest scale at which $E_2(d,t) = 1$ decreases with time indicating the production of smaller and smaller liquid structures and, consequently, the increase of the system specific-surface. Note that since atomization process is not completed at the bottom of the image (see Fig. 2), $E_2(d,t)$ remains time-dependent at the larger times. In the small scale range, Fig. 5 reports a linear behavior at all times. Being a log-log representation, this figure is a Richardson-Mandelbrot plot and this linear behavior denotes a fractal behavior whose dimension in the present case is close to 1. This value comes from the fact that the surface area removed by the erosion operation for small scales d is proportional to d (it is equal to $L_M d$ where L_M is the interface length or the perimeter of the system). This result agrees with the behavior described by the scale entropy diffusion model (see Section 2).

The measurement of the cumulative function $E_2(d,t)$ incorporates the determination of the local system surface area ($S_T(t)$ in Eq.(9)) and allows calculating the interface length ($L(t) = 2S_T(t)e_2(0,t)$). The mean interface length and surface area, $L_M(t)$ and $S_M(t)$ respectively, are shown in Fig. 6. The interface length increases with time and saturates at an asymptotic value (Fig. 6-a). The result for ΔP_i = 0.1 MPa displays a slight decrease of L_M at long time. As observed in other situations [18], this reduction is likely the mark of an interface loss during the final step of the atomization process. The limited visualization field of the experiments did not allow catching this behavior for the other injection pressures. Figure 6-a shows that the temporal evolution of the interface length is exponential at initial times. The slope of the initial linear behavior shown in Fig. 6-a represents the growth rate of L_M. This growth rate increases with the injection pressure and, as shown in Fig. 7, correlates with the issuing liquid flow Reynolds number *Re*. This result underlines the dominant role of the liquid flow in its initial deformation. We note in Fig. 7 that the result at ΔP_i = 0.1 MPa escapes from the behavior reported by the other injection pressures. This difference denotes a different primary atomization process for the lowest injection pressure likely due to an insufficient development of liquid turbulence. For this reason, this case is eliminated in the rest of the analysis.

The evolution of the mean surface area S_M depends on the injection pressure (see Fig. 6-b). For small ΔP_i, S_M decreases and reaches an asymptotic value. For medium ΔP_i (0.5 and 0.6 MPa) this behavior is preceded by a slight increase and the asymptotic value is not reached. For high ΔP_i, the initial increase is very much pronounced. The initial increase of S_M illustrates a more and more perturbed state of the liquid jet. Indeed, the line-of-sight nature of the visualization diagnostic does not allow initial highly perturbed jets to be fully resolved, and their 2D projection is mainly sensitive to the jet radial expansion, which is perceived as an increasing surface area S_M. The subsequent decrease of S_M occurs when the liquid

fragments produced during the process and their own evolution become observable by the imaging diagnostic.

An example of the temporal evolution of the scale diameter $D(d,t)$ (Eq. (10)) for a series of scale d is shown in Fig. 8 (ΔP_i = 0.4 MPa). For this injection pressure, the first AW position corresponds to the time t = 146 µs. For the scale d = 0, the scale diameter continuously decreases with time. As said above, this behavior indicates that the system shape variation is undergone at d = 0 as an elongation mechanism, which synthetizes the increase of the interface length per unit surface area during the atomization process. The temporal evolution of the scale diameter is investigated by considering an exponential dependence with time that introduces the variation-rate $\alpha(d,t)$:

$$D(d,t) \propto \exp\left(-\alpha(d,t)t\right) \tag{11}$$

The elongation mechanism identified for the scale d = 0 is associated to a positive variation-rate, i.e., $\alpha(0,t) > 0$. We see in Fig. 8 that, at initial times, $\alpha(0,t)$ is independent of the time. It is therefore noted $\alpha(0)$. This specific period of time (140 µs-200 µs for ΔP_i = 0.4 MPa) roughly corresponds to the one during which the growth rate of L_M is constant. Similar observations are made for the other injection pressures. Therefore, as for the growth-rate of L_M, the initial elongation characteristic time 1/ $\alpha(0)$ correlates with the jet Reynolds number. This behavior is illustrated in Fig. 9 from which the correlation $\alpha(0) \propto Re^{1.28}$ is obtained. This result says that the initial elongation mechanism undergone at d = 0 is imposed by the complex internal liquid flow dynamics.

When time increases, Fig. 8 shows that the variation-rate $\alpha(0,t)$ continuously decreases. In other words, the characteristic time 1/ $\alpha(0,t)$ of the elongation mechanism increases. This

behavior is illustrated in Fig. 10 for four injection pressures. After a period of time during which $1/\alpha(0,t)$ is constant, it increases linearly with the time. This increase begins sooner when the injection pressure increases and appears very similar from one injection pressure to another. It indicates a less and less effective elongation mechanism in terms of interface specific-length production. Figure 10 also shows the temporal evolution of the characteristic capillary time T_σ defined as:

$$T_\sigma = \sqrt{\frac{\rho_L D(0,t)^3}{\sigma}} \tag{12}$$

The capillary characteristic time decreases with time because of the continuous decrease of the scale diameter $D(0,t)$ (Fig. 8). We see in Fig. 10 that, for every injection pressure, the characteristic elongation time increases when it becomes of the order of the capillary characteristic time T_σ. This shows that the loss of elongation mechanism efficiency illustrated by a continuous increase of the $1/\alpha(0,t)$ is due to surface tension effects. This result underlines the relevance of the time T_σ (Eq. (12)) as well as the use of the scale diameter $D(0,t)$ to evaluate a pertinent capillary characteristic time.

These results suggest the existence of two phases in the jet atomization process. During the first phase, the elongation mechanism has a constant variation rate that correlates with the jet Reynolds number. The mechanism is therefore controlled by the jet internal dynamics. During the second phase, the elongation mechanism has a linearly increasing characteristic time and this increase is independent of the jet Reynold number. The liquid jet is not subject to its internal dynamics anymore and it relaxes according to a mechanism mainly controlled by the surface tension forces. The transition from phase 1 to phase 2 occurs when $1/\alpha(0,t)$ and T_σ are of the same order of magnitude. Using Eqs. (11) and (12), this condition writes:

$$\frac{\rho_L\left(\frac{\mathrm{d}D(0,t)}{\mathrm{d}t}\right)^2 D(0,t)}{\sigma} \approx 1 \qquad (13)$$

Equation (13) introduces a new time-dependent Weber number based of the scale diameter $D(0,t)$. In the first phase, this number is greater than 1 and it becomes less than 1 in the second phase.

Figure 8 also shows that whereas $D(0,t)$ decreases continuously with time, this is not the case for other scales. The scale diameters of the larger scales (between 200 µm and 300 µm) increase continuously with time, and those for intermediate scales (around 100 µm) may decrease first and then increase. Thus, the perception of the system temporal evolution depends on the scale. At the same instant, small scales undergo an elongation mechanism whereas larger scales undergo a contraction mechanism. The ranges of scales undergoing elongation or contraction vary with time. This point is evidenced in Fig. 11 where the variation rates $\alpha(d,t)$ are shown as a function of d for several times (ΔP_i = 0.4 MPa). At each time, $\alpha(d,t)$ continuously decreases with the scale, starting at a positive value for $d = 0$ to end at a negative value for the largest scale. As said above, the scales for which $\alpha(d,t)$ is positive are those undergoing an elongation, whereas those with a negative $\alpha(d,t)$ undergo a contraction. The scale space is thus divided in two regions: the small scale region associated to $\alpha(d,t) > 0$ and the large scale region associated to $\alpha(d,t) < 0$. The temporal evolution of these two regions describes the atomization process. We see that the large scale region enlarges to the detriment of the small scale region. Furthermore, in the small scale region, $\alpha(d,t)$ decreases as a function of t for a given scale d whereas in the large scale region $|\alpha(d,t)|$ increases. This says that during the atomization process the elongation mechanism decreases

in strength and concerns less and less scales, whereas the contraction mechanism is more and more effective and concerns an enlarging scale interval. The contraction mechanism diffuses in the space scale. This diffusion process can be characterized by considering the temporal evolution of the specific scale $d_0(t)$ for which, at each time, $\alpha(d_0,t) = 0$. The scale $d_0(t)$ is understood as the one not influenced by the system shape variation at time t.

Figure 12 shows the specific scale $d_0(t)$ for five injection pressures. As expected from Fig.11, this scale decreases with time and the decreasing rate increases with the injection pressure. For $\Delta P_i = 0.2$ MPa, d_0 initiates an increase at large times. This behavior seems to be associated with the breakup region. For these times, the small scale ($d < d_0$) elongation rate becomes almost equal to zero. The increase of d_0 with time illustrates the progressive reduction of the effect of the contraction mechanism. At the end of the process, d_0 tends towards infinity and $\alpha(d,t) = 0$ for all scales. This part of the process could not be investigated in detail here because the breakup region was not visualized for the injection pressure larger than 0.2 MPa.

An attempt of modeling the scale diffusion mechanism characterized by $d_0(t)$ is performed by using Eq. (2). For every injection pressure this equation is applied in the scale range $d_0(t=0)$ to $d_0(t)$, i.e., $x = \ln(d_0(t)/d_0(0))$. We assume here that at $t = 0$, the specific scale $d_0(0)$ is equal to the injector discharge orifice diameter d_{or}. Note that this assumption agrees relatively well with the results shown in Fig. 12. This suggests that at the initial time, all existing scales undergo an elongation mechanism. The characteristic time corresponding to the scale range $[d_0(t); d_0(0)]$ is the time t. Rearranging Eq. (2) yields:

$$\ln\left|\ln\left(\frac{d_0(t)}{d_0(0)}\right)\right| = \frac{1}{2}\left(\ln(t) + \ln(\chi)\right) \tag{14}$$

The elements of Eq. (14) are plotted in Fig. 13 for four injection pressures. The resulting curves show two regions, each of them reporting a rather linear behavior. These regions correspond to the two phases of the process identified in Fig. 10, i.e., the internal dynamics mechanism phase and the relaxation mechanism phase. (These two phases are noted in Fig. 13.) For every injection pressure, the linear behavior of the second region displays a slope equal to ½ in agreement with Eq. (14) (see Fig. 13) indicating that the evolution of the scale d_0 follows the diffusion expressed by the scale entropy diffusion model. According to Eq. (14), it is therefore possible to evaluate the scale diffusivity for every injection pressure by considering the value at the origin of the curves shown in Fig. 13. The results of this evaluation are presented in Fig. 14 as a function of the injection pressure. This figure shows that for an injection pressure up to 1.5 MPa, the scale diffusivity linearly depends on the injection pressure. This result agrees with the one found in a previous investigation [9]. For larger injection pressures, the scale diffusivity still increases but the linear dependence is lost. This behavior may be due to the modification of the atomization process for these pressures because of the action of the aerodynamic forces. Further work is required to confirm this point.

5 Conclusion

In the present paper, the scale diffusion mechanism of the atomization process of a jet emanating from a GDI injector has been achieved. The experimental work is limited to low injection pressures in order to maintain a sufficiently visible atomization process and to produce well spatially resolved images of it. The analysis is based on a multi-scale description of the process by measuring the local cumulative scale distribution $E_2(d,t)$ and its temporal evolution and by analyzing the scale diameter $D(d,t)$ defined as the inverse of the first derivative of $E_2(d,t)$ in the scale space. The temporal variation of this diameter indicates

whether the scale undergoes an elongation or a contraction mechanism. The main conclusions provided by this analysis are the following.

At each instant of the process, the scale space is divided in two regions, i.e., the small-scale region corresponding to the scales that undergo an elongation mechanism and the large-scale region corresponding to the scales that undergo a contraction mechanism. The atomization process can be described as a succession of liquid structure formation and deformation. The production of liquid structures is associated to a mechanism of elongation. The deformation of these structures implies a contraction at their greater scales and an elongation at their small scales favoring the production of smaller structures on which the process repeats. This elongation-contraction mechanism diffuses therefore in the small-scale region. Furthermore the evolution rate of the elongation mechanism diminishes with time and the whole process is completed when this rate is equal to zero. As far as the elongation mechanism is concerned, it is found that it is controlled by the liquid jet dynamic at earlier times and by surface tension at later times defining two phases in the atomization process. During the first phase, the evolution rate of the elongation mechanism is constant with time and correlates with the jet Reynolds number. In the second phase, the inverse of this evolution rate linearly increases with time in a way that appears independent of the injection pressure. A temporal Weber number to identify the phase transition has been established. It is greater than 1 in the first phase and less than 1 in the second phase.

The elongation-contraction diffusion mechanism is characterized by the temporal evolution of the scale that is not influenced by the system shape variation at time t. This scale decreases with time and it is found that its variation during the second phase of the atomization process allows determining the scale diffusivity introduced by the scale entropy diffusion model. In agreement with previous results it is found here that the scale diffusivity increases linearly

with the injection pressure when it is low. For higher injection pressures, this linearly dependency is lost for a reason that has not been identified here.

These different results demonstrate the interest of the multi-scale description of liquid atomization process and of the scale entropy diffusion theory to model this phenomenon. Such developments bring a different view of this complex problem and do participate to improve our understanding and our capability to model them. Furthermore, these new concepts can find interesting connections with direct numerical simulation. For instance, they can be used to provide validation procedure based on different characteristics that those usually in use for this purpose. Furthermore, the direct numerical simulation offers an affordable way to perform a 3D multi-scale analysis of atomization processes. Indeed, the 2D approach presented here can be easily extended to 3D introducing the volume-based scale distribution. These aspects are under consideration in our group. Finally, in the future, the scale entropy theory might provide a new equation to model the final breakup phase which is always controlled by the mesh size in direct numerical simulation codes.

6 Acknowledgments

The authors acknowledge the financial support from the French National Research Agency (ANR) through the program *Investissements d'Avenir* (ANR-10 LABX-09-01), LABEX EMC3.

7 References

1. B. Mandelbrot, The fractal geometry of nature. WH Freeman & Co, New-York (1982).
2. U. Shavit, N. Chigier, Atom. Sprays. 5 (1995) 525-543.
3. S. Grout, C. Dumouchel, J. Cousin, H. Nuglisch, Int. Journ. Multiphase Flows 33 (2007) 1023-1044.

4. D. Queiros-Conde, Proc. R. Soc. Lon. A. 459 (2003) 3043-3059.
5. D. Queiros-Conde, Physical Review E, 64, 015301(R).
6. D. Queiros-Conde, M. Feidt, JETC IX, 12-15 June 2007, Ecole Nationale Supérieure des Mines de Saint-Etienne, France.
7. D. Queiros-Conde, F. Foucher, C. Mounaïm-Rousselle, H. Kassem, M. Feidt, Physica A 387 (2008) 6712-6724.
8. L. Le Moyne, V. Freire, D. Queiros-Conde, Chaos, Solitons and Fractals 38 (2008) 696-704.
9. C. Dumouchel, S. Grout, Int. J. Multiphase Flows 35 (2009) 952-962.
10. C. Dumouchel, S. Grout, Physica A, 390 (2011) 1811-1825.
11. C. Dumouchel, J.B. Blaisot, ILASS-Europe 2013, Chania (Greece), September 2013
12. C. Dumouchel, J. Cousin, S. Grout, Journ. of Flow Visualization & Image Processing 15 (2008) 59-83.
13. J. Bérubé, M. Jébrak, Computers & Geosciences. 25 (1999) 1059-1.
14. L.W. Evers, SAE Technical Series (1994) Paper n°940190.
15. C. Dumouchel, J.B. Blaisot, E. Bouche, T. Ménard, T.T. Vu, International Journ. Multiphase Flow 73 (2015) 251-263.
16. C. Clasen, P.M. Phillips, L. Palengetic, J. Vermant, AIChE Journal, 58 (2012)3242-3255.
17. C. Dumouchel, N. Leboucher, D. Lisiecki, Exp. In Fluids. 54 (2013) 1554(1-17).
18. R. Andersson, A. Helmi, Applied Math. Mod. 38 (2014) 4186-4196.

Figure Captions

Figure 1: Raw image of the liquid flow issuing from the injector. From top left to bottom right: 0.1 MPa, 0.2 MPa, 0.3 MPa, 0.4 MPa, 0.5 MPa, 0.6 MPa, 1.5 MPa, 2.0 MPa, 2.5 MPa.

Figure 2: Two gray-level reoriented images of the liquid flow issuing from the injector. From top left to bottom right: 0.1 MPa, 0.2 MPa, 0.3 MPa, 0.4 MPa, 0.5 MPa, 0.6 MPa, 1.5 MPa, 2.0 MPa, 2.5 MPa.

Figure 3: Illustration of the Analyzing Window (the gray rectangle), of its position h and of the equivalent time t. (On scale.)

Figure 4: Local cumulative scale distribution measurement: The portion of the liquid system delimited by the Analyzing window has an area equal to $S_T(t)$. It is eroded with a circular structuring element of diameter d (gray circle in the figure). The erosion step erases the hashed surface. The remaining surface area is $S(d,t)$ (white surface in the figure). The erosion operation is performed for d ranging from 0 to infinity.

Figure 5: Temporal evolution of the cumulative scale function $E_2(d,t)$ (ΔP_i = 0.4 MPa)

Figure 6: a – Temporal evolution of the mean interface length L_M, **b -** Temporal evolution of the mean surface area S_M

Figure 7: Growth-rate of the mean interface length L_M at small times as a function of the Reynolds number Re

Figure 8: Temporal evolution of the scale diameter $D(d,t)$ (ΔP_i = 0.4 MPa, The scale increment between two consecutive curves is 11.6 µm)

Figure 9: Characteristic time of the initial elongation rate of the interface (d = 0) as a function of the Reynolds number Re

Figure 10: Temporal evolution of the elongation rate of the interface ($d = 0$) and comparison with the characteristic capillary time (several injection pressures)

Figure 11: Variation-rate of the scale diameter according to the scale for several times **(**ΔPi = 0.4 MPa, The time increment between two consecutive curves is 13.4 µs)

Figure 12: Temporal evolution of the scale d_0

Figure 13: Illustration of Eq. (13) for four injection pressures (The dot line roughly delimits phase 1 and phase 2 of the atomization process)

Figure 14: The scale diffusivity as a function of the injection pressure

Figure

Fig. 1

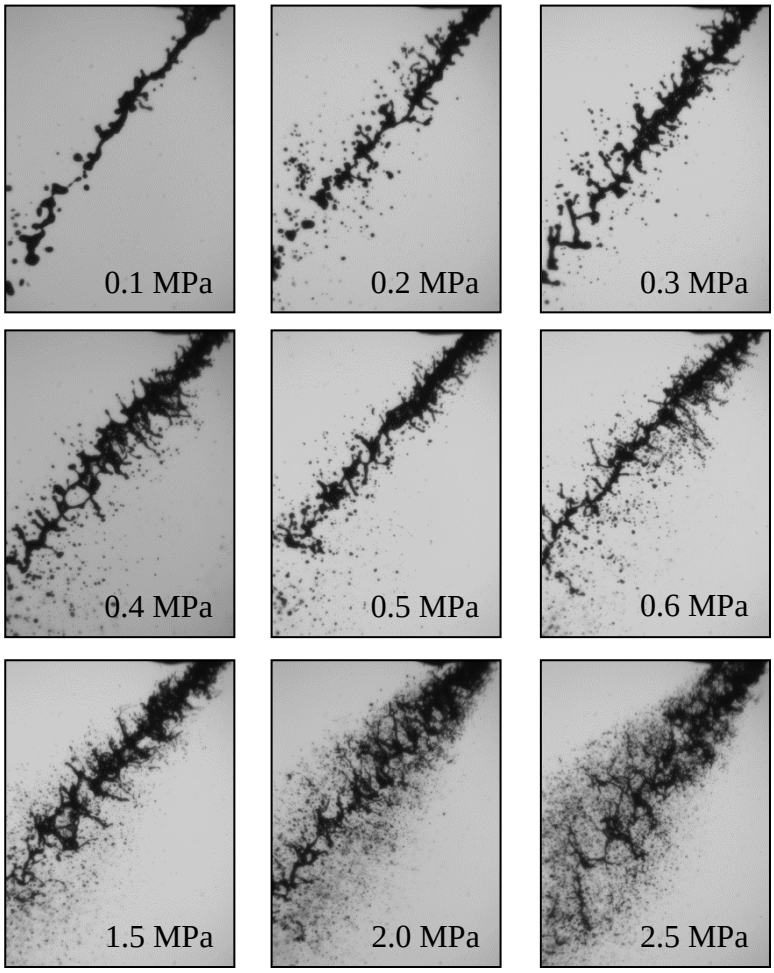

Figure

Fig. 2

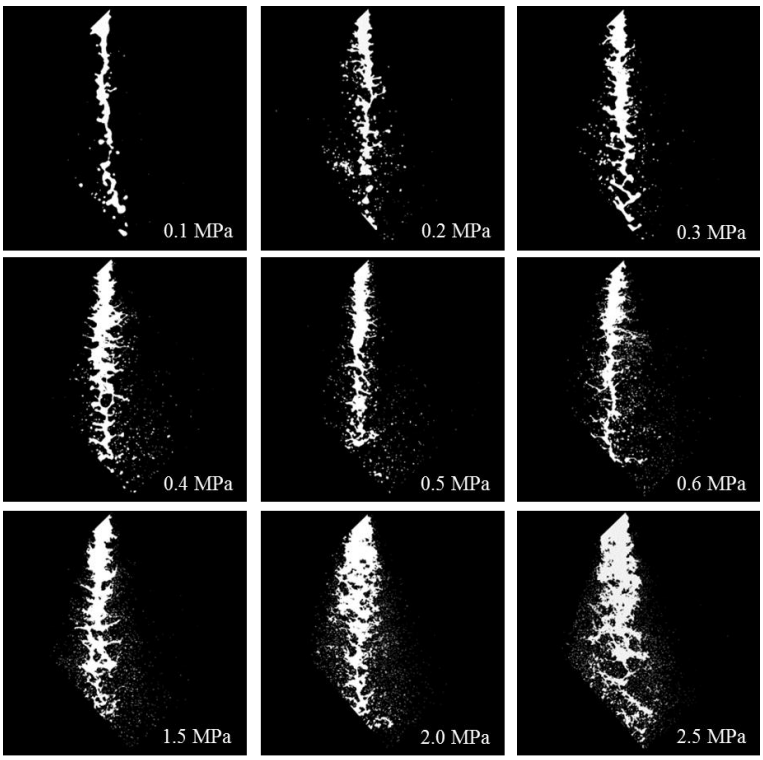

Figure

Fig. 3

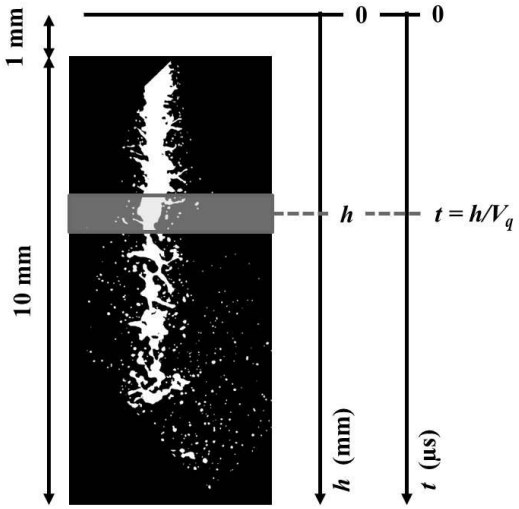

Figure

Fig. 4

Figure

Fig. 5

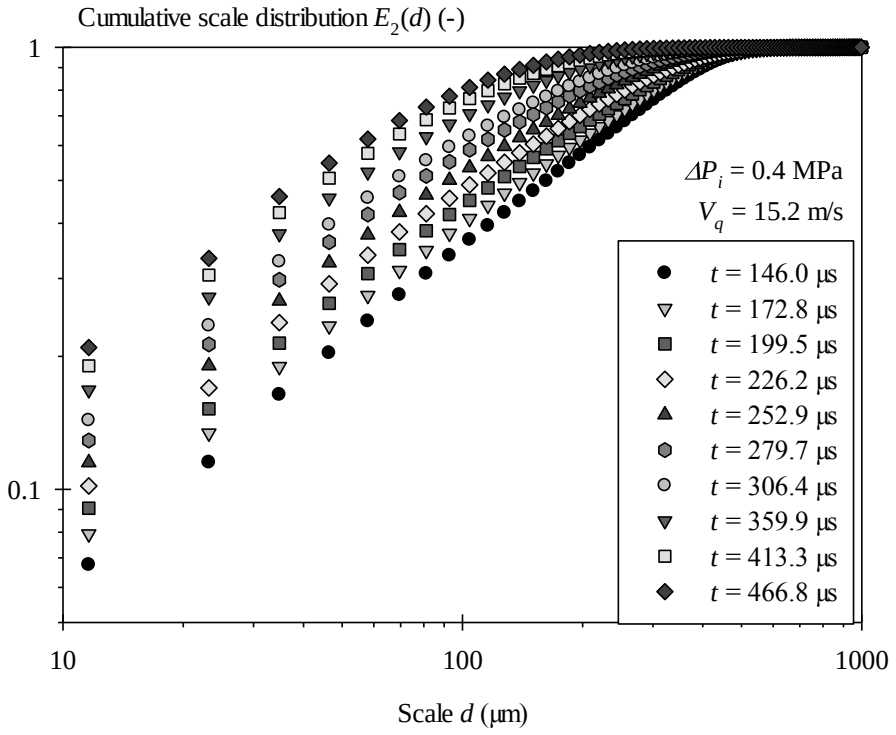
Cumulative scale distribution $E_2(d)$ (-)
1
0.1
10
100
1000
Scale d (μm)
ΔP_i = 0.4 MPa
V_q = 15.2 m/s
t = 146.0 μs
t = 172.8 μs
t = 199.5 μs
t = 226.2 μs
t = 252.9 μs
t = 279.7 μs
t = 306.4 μs
t = 359.9 μs
t = 413.3 μs
t = 466.8 μs

Figure

Fig. 6-a

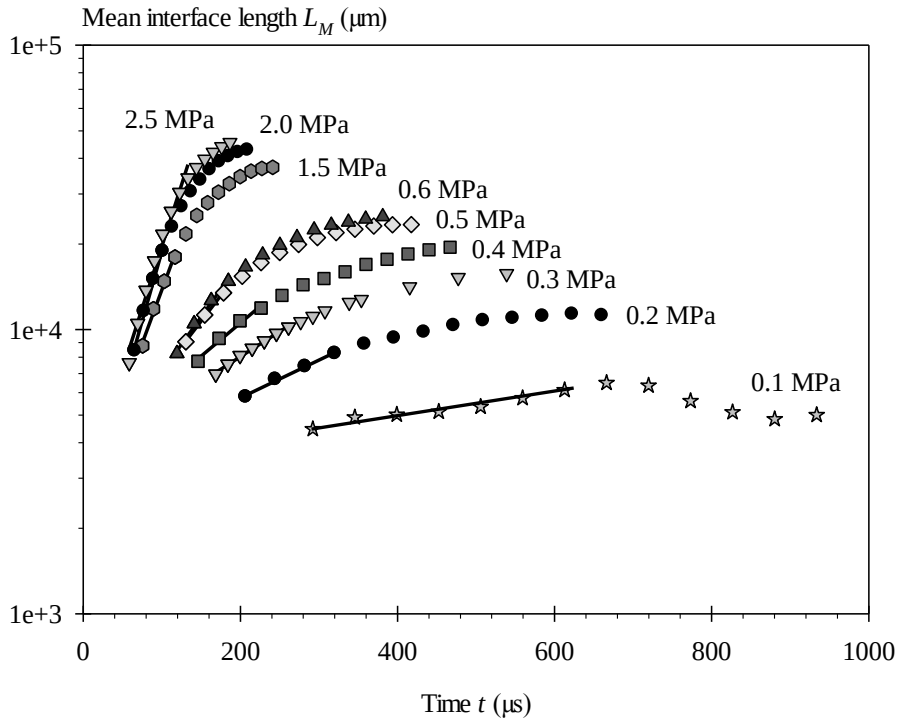

Figure

Fig. 6-b

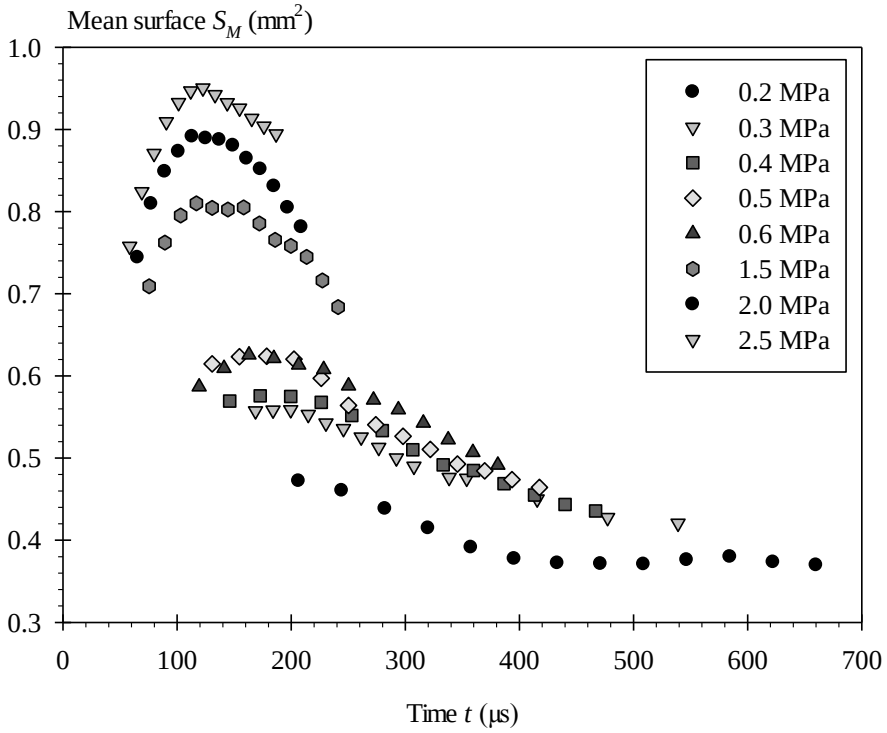

Figure

Fig. 7

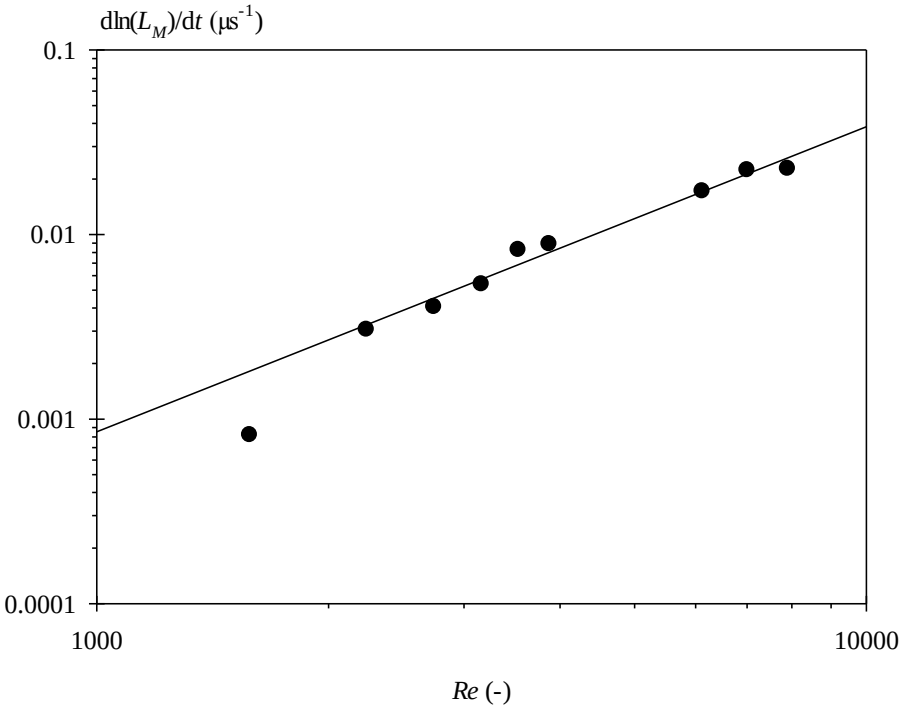

Figure

Fig. 8

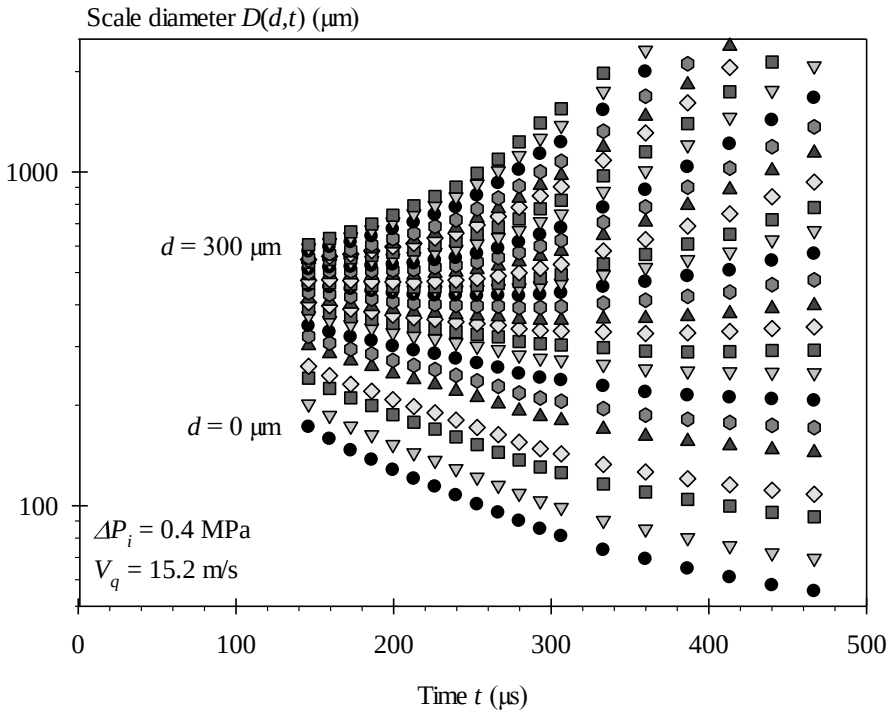
Scale diameter $D(d,t)$ (μm)
1000
100
d = 300 μm
d = 0 μm
ΔP_i = 0.4 MPa
V_q = 15.2 m/s
0
100
200
300
400
500
Time t (μs)

Figure

Fig. 9

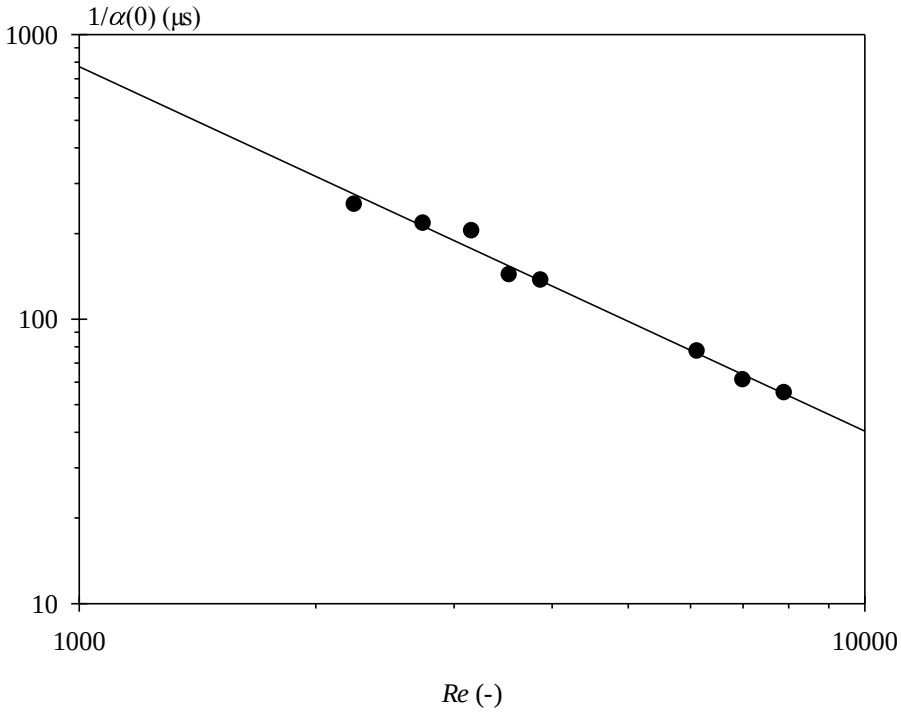

Figure

Fig. 10

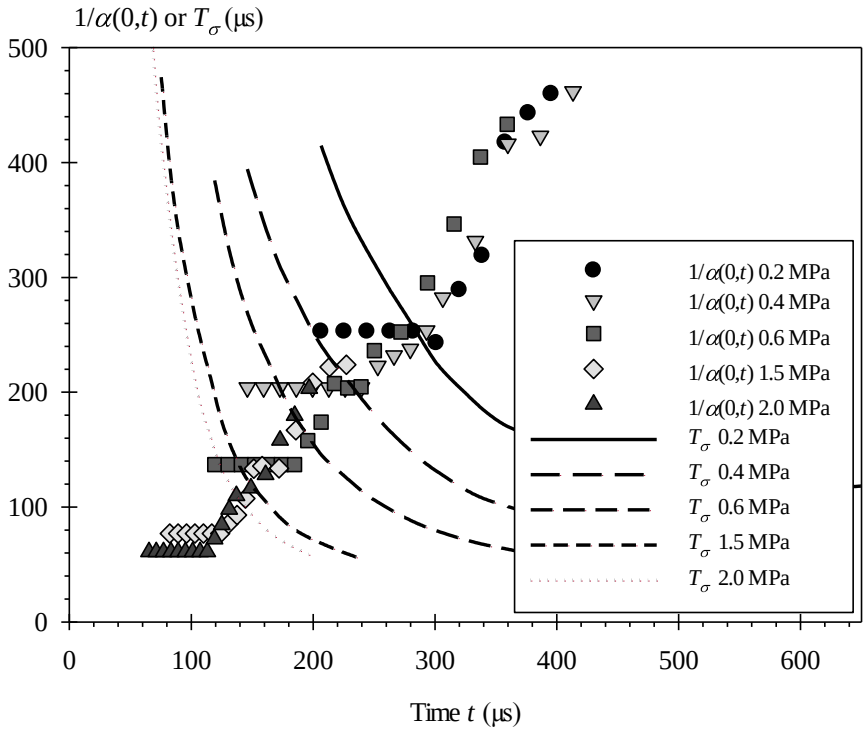

Figure

Fig. 11

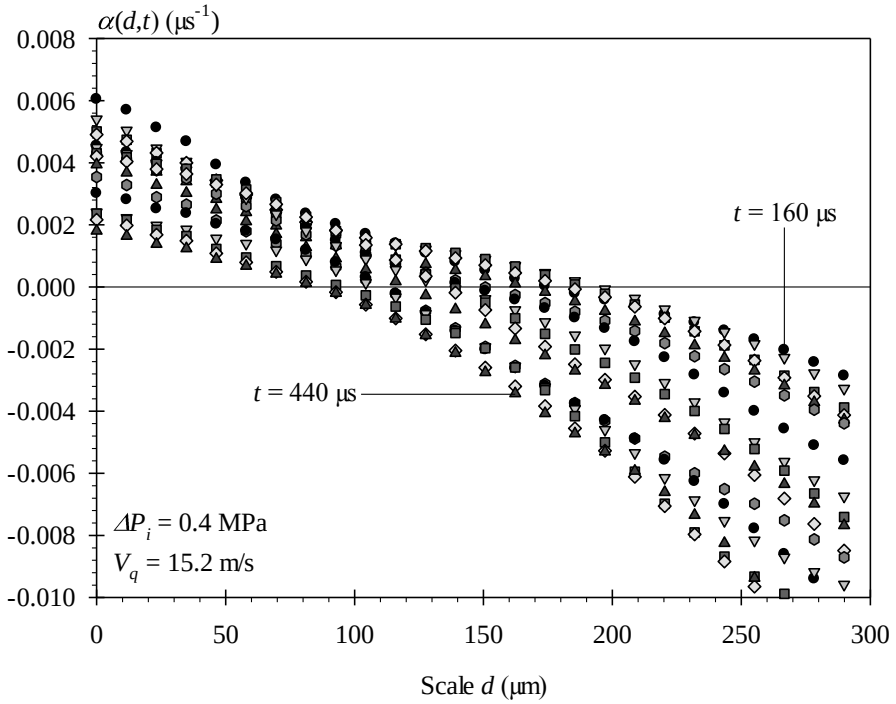

Figure

Fig. 12

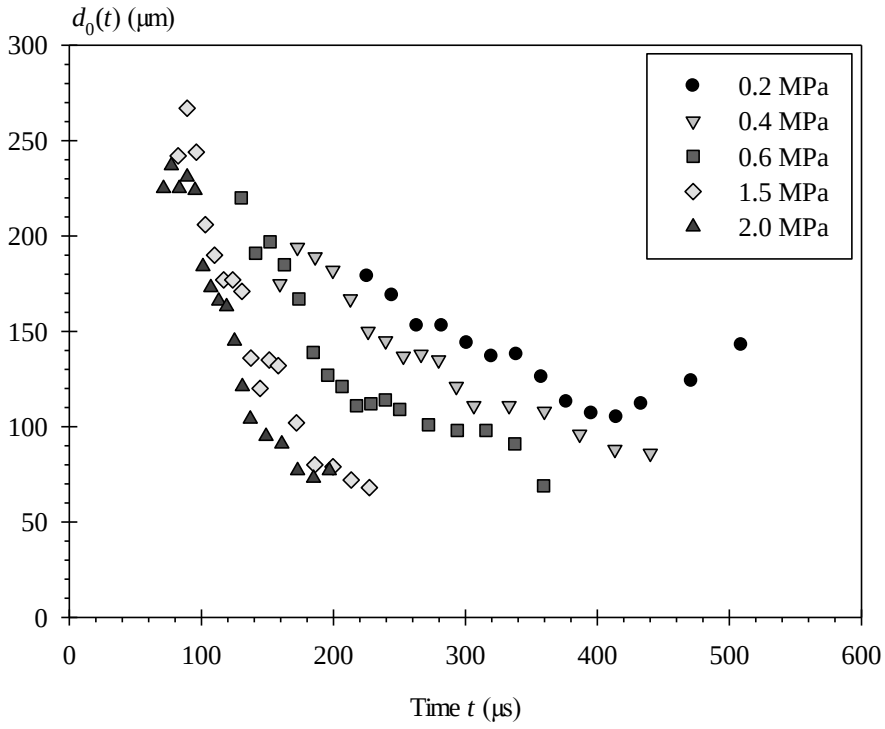

Figure

Fig. 13

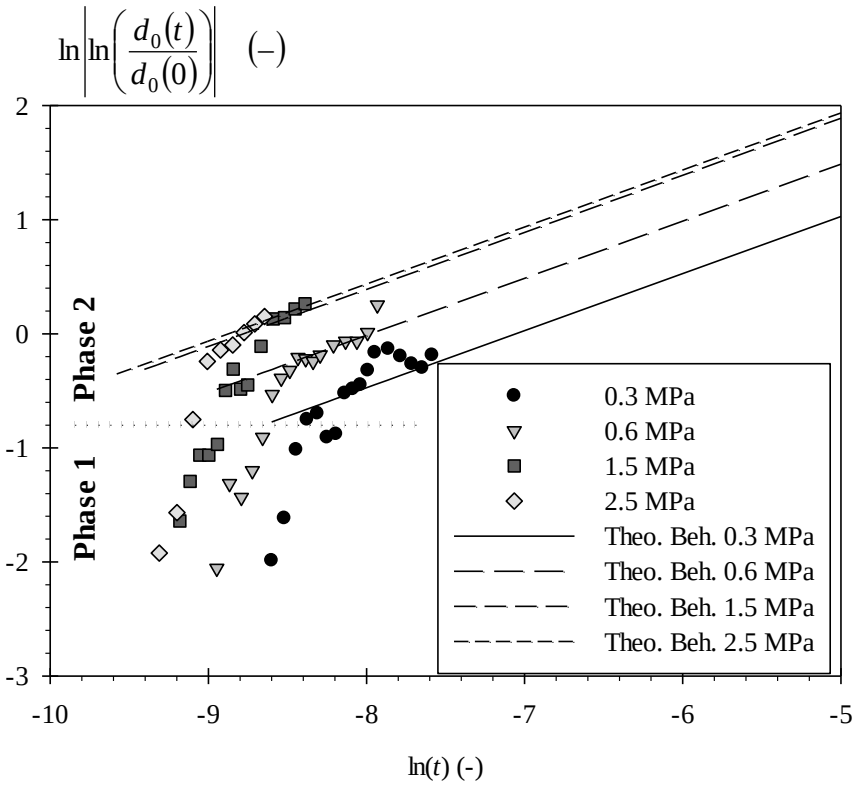

Figure

Fig. 14